# Automated choroidal neovascularization detection algorithm for optical coherence tomography angiography

**Li Liu,[1,2] Simon S. Gao,[1] Steven T. Bailey,[1] David Huang,[1] Dengwang Li,[2,*] and Yali Jia[1,*]**

[1]*Casey Eye Institute, Oregon Health & Science University, Portland, Oregon, USA*
[2]*College of Physics and Electronics, Shandong Normal University, Jinan, China*
[*]*jiaya@ohsu.edu*

**Abstract:** Optical coherence tomography angiography has recently been used to visualize choroidal neovascularization (CNV) in participants with age-related macular degeneration. Identification and quantification of CNV area is important clinically for disease assessment. An automated algorithm for CNV area detection is presented in this article. It relies on denoising and a saliency detection model to overcome issues such as projection artifacts and the heterogeneity of CNV. Qualitative and quantitative evaluations were performed on scans of 7 participants. Results from the algorithm agreed well with manual delineation of CNV area.

## References and links

1. D. Pascolini, S. P. Mariotti, G. P. Pokharel, R. Pararajasegaram, D. Etya'ale, A.-D. Négrel, and S. Resnikoff, "2002 global update of available data on visual impairment: a compilation of population-based prevalence studies," Ophthalmic Epidemiol. **11**(2), 67–115 (2004).
2. R. D. Jager, W. F. Mieler, and J. W. Miller, "Age-related macular degeneration," N. Engl. J. Med. **358**(24), 2606–2617 (2008).
3. P. T. de Jong, "Age-related macular degeneration," N. Engl. J. Med. **355**(14), 1474–1485 (2006).
4. L. A. Donoso, D. Kim, A. Frost, A. Callahan, and G. Hageman, "The role of inflammation in the pathogenesis of age-related macular degeneration," Surv. Ophthalmol. **51**(2), 137–152 (2006).
5. P. E. Stanga, J. I. Lim, and P. Hamilton, "Indocyanine green angiography in chorioretinal diseases: indications and interpretation: an evidence-based update," Ophthalmology **110**(1), 15–23 (2003).
6. M. P. López-Sáez, E. Ordoqui, P. Tornero, A. Baeza, T. Sainza, J. M. Zubeldia, and M. L. Baeza, "Fluorescein-induced allergic reaction," Ann. Allergy Asthma Immunol. **81**(5), 428–430 (1998).
7. D. Huang, E. A. Swanson, C. P. Lin, J. S. Schuman, W. G. Stinson, W. Chang, M. R. Hee, T. Flotte, K. Gregory, C. A. Puliafito, and et, "Optical coherence tomography," Science **254**(5035), 1178–1181 (1991).
8. L. An and R. K. Wang, "In vivo volumetric imaging of vascular perfusion within human retina and choroids with optical micro-angiography," Opt. Express **16**(15), 11438–11452 (2008).
9. Y. Yasuno, Y. Hong, S. Makita, M. Yamanari, M. Akiba, M. Miura, and T. Yatagai, "In vivo high-contrast imaging of deep posterior eye by 1-microm swept source optical coherence tomography and scattering optical coherence angiography," Opt. Express **15**(10), 6121–6139 (2007).
10. I. Grulkowski, I. Gorczynska, M. Szkulmowski, D. Szlag, A. Szkulmowska, R. A. Leitgeb, A. Kowalczyk, and M. Wojtkowski, "Scanning protocols dedicated to smart velocity ranging in spectral OCT," Opt. Express **17**(26), 23736–23754 (2009).
11. J. Fingler, R. J. Zawadzki, J. S. Werner, D. Schwartz, and S. E. Fraser, "Volumetric microvascular imaging of human retina using optical coherence tomography with a novel motion contrast technique," Opt. Express **17**(24), 22190–22200 (2009).
12. G. Liu, W. Qi, L. Yu, and Z. Chen, "Real-time bulk-motion-correction free Doppler variance optical coherence tomography for choroidal capillary vasculature imaging," Opt. Express **19**(4), 3657–3666 (2011).
13. Y. Jia, O. Tan, J. Tokayer, B. Potsaid, Y. Wang, J. J. Liu, M. F. Kraus, H. Subhash, J. G. Fujimoto, J. Hornegger, and D. Huang, "Split-spectrum amplitude-decorrelation angiography with optical coherence tomography," Opt. Express **20**(4), 4710–4725 (2012).

14. S. S. Gao, G. Liu, D. Huang, and Y. Jia, "Optimization of the split-spectrum amplitude-decorrelation angiography algorithm on a spectral optical coherence tomography system," Opt. Lett. **40**(10), 2305–2308 (2015).
15. Y. Jia, S. T. Bailey, D. J. Wilson, O. Tan, M. L. Klein, C. J. Flaxel, B. Potsaid, J. J. Liu, C. D. Lu, M. F. Kraus, J. G. Fujimoto, and D. Huang, "Quantitative optical coherence tomography angiography of choroidal neovascularization in age-related macular degeneration," Ophthalmology **121**(7), 1435–1444 (2014).
16. Y. Jia, S. T. Bailey, T. S. Hwang, S. M. McClintic, S. S. Gao, M. E. Pennesi, C. J. Flaxel, A. K. Lauer, D. J. Wilson, J. Hornegger, J. G. Fujimoto, and D. Huang, "Quantitative optical coherence tomography angiography of vascular abnormalities in the living human eye," Proc. Natl. Acad. Sci. U.S.A. **112**(18), E2395–E2402 (2015).
17. T. E. de Carlo, M. A. Bonini Filho, A. T. Chin, M. Adhi, D. Ferrara, C. R. Baumal, A. J. Witkin, E. Reichel, J. S. Duker, and N. K. Waheed, "Spectral-domain optical coherence tomography angiography of choroidal neovascularization," Ophthalmology **122**(6), 1228–1238 (2015).
18. R. F. Spaide, "Optical coherence tomography angiography signs of vascular abnormalization with antiangiogenic therapy for choroidal neovascularization," Am. J. Ophthalmol. **160**(1), 6–16 (2015).
19. L. Kuehlewein, S. R. Sadda, and D. Sarraf, "OCT angiography and sequential quantitative analysis of type 2 neovascularization after ranibizumab therapy," Eye (Lond) (2015).
20. Y. Jia, E. Wei, X. Wang, X. Zhang, J. C. Morrison, M. Parikh, L. H. Lombardi, D. M. Gattey, R. L. Armour, B. Edmunds, M. F. Kraus, J. G. Fujimoto, and D. Huang, "Optical coherence tomography angiography of optic disc perfusion in glaucoma," Ophthalmology **121**(7), 1322–1332 (2014).
21. M. F. Kraus, J. J. Liu, J. Schottenhamml, C. L. Chen, A. Budai, L. Branchini, T. Ko, H. Ishikawa, G. Wollstein, J. Schuman, J. S. Duker, J. G. Fujimoto, and J. Hornegger, "Quantitative 3D-OCT motion correction with tilt and illumination correction, robust similarity measure and regularization," Biomed. Opt. Express **5**(8), 2591–2613 (2014).
22. A. F. Frangi, W. J. Niessen, K. L. Vincken, and M. A. Viergever, "Multiscale vessel enhancement filtering," in *Medical Image Computing and Computer-Assisted Intervention* (Springer, MICCAI, 1998), pp. 130–137.
23. M. W. Law and A. C. Chung, "Three dimensional curvilinear structure detection using optimally oriented flux," in *Computer Vision–ECCV 2008,* (Springer, 2008), pp. 368–382.
24. D. Chen and L. D. Cohen, "Piecewise geodesics for vessel centerline extraction and boundary delineation with application to retina segmentation," in *Scale Space and Variational Methods in Computer Vision,* (Springer, SSVM, 2015), pp. 270–281.
25. A. Borji and L. Itti, "State-of-the-art in visual attention modeling," IEEE Trans. Pattern Anal. Mach. Intell. **35**(1), 185–207 (2013).
26. O. Tan, G. Li, A. T. Lu, R. Varma, and D. Huang; Advanced Imaging for Glaucoma Study Group, "Mapping of macular substructures with optical coherence tomography for glaucoma diagnosis," Ophthalmology **115**(6), 949–956 (2008).
27. S. Goferman, L. Zelnik-Manor, and A. Tal, "Context-aware saliency detection," IEEE Trans. Pattern Anal. Mach. Intell. **34**(10), 1915–1926 (2012).
28. L. Itti, C. Koch, and E. Niebur, "A model of saliency-based visual attention for rapid scene analysis," IEEE Trans. Pattern Anal. Mach. Intell. **20**(11), 1254–1259 (1998).
29. C. Tomasi and R. Manduchi, "Bilateral filtering for gray and color images," in *Sixth International Conference on Computer Vision,* (IEEE, Bombay, 1998), pp. 839–846.
30. J. Lee, N. Kim, H. Lee, J. B. Seo, H. J. Won, Y. M. Shin, Y. G. Shin, and S.-H. Kim, "Efficient liver segmentation using a level-set method with optimal detection of the initial liver boundary from level-set speed images," Comput. Methods Programs Biomed. **88**(1), 26–38 (2007).
31. B. Lumbroso, D. Huang, C. C. Chen, Y. Jia, M. Rispoli, A. Romano, and N. K. Waheed, *Clinical OCT Angiography Atlas* (Jaypee Brothers Medical Publishers, 2015).
32. Y. Huang, Q. Zhang, and R. K. Wang, "Efficient method to suppress artifacts caused by tissue hyper-reflections in optical microangiography of retina in vivo," Biomed. Opt. Express **6**(4), 1195–1208 (2015).

## 1. Introduction

Age-related macular degeneration (AMD) is the leading cause of blindness in people 50 years or older in the developed world [1, 2]. The advanced, neovascular form of AMD is characterized by the presence of choroidal neovascularization (CNV), pathologic new vessels from the choroid that grow into the avascular outer retina through breaks in Bruch's membrane (BM). CNV can lead to subretinal hemorrhage, fluid exudation, lipid deposition, detachment of the retinal pigment epithelium from the choroid, fibrotic scars, or a combination of these findings that result in vision loss [2–5]. Fluorescein (FA) and/or indocyanine green angiography (ICGA) have traditionally been used to detect and assess CNV in the clinic. These techniques are however 2-dimensional (2D) and involve intravenous dye injections, which can lead to nausea and anaphylaxis [6].

Optical coherence tomography (OCT) is a noninvasive, depth resolved, volumetric imaging technique that is commonly used to visualize retinal morphology [7]. However, conventional structural OCT is not able to detect blood flow and discriminate vascular tissue from its surroundings. To overcome this limitation, several OCT angiography methods have been proposed to identify blood flow at the microcirculation level [8–12]. We developed the split-spectrum amplitude-decorrelation angiography (SSADA) algorithm to distinguish blood flow from static tissues based on detecting the reflectance amplitude decorrelation over consecutive cross-sectional B-scans at the same location [13, 14]. Segmentation of SSADA based OCT angiograms can identify CNV as blood flow in the outer retina, a region devoid of blood flow in healthy eyes [15–19]. Accurate detection and quantification of CNV would be extremely useful to the clinicians in the diagnosis and evaluation of the therapeutic effect of different treatments. Manual delineation from experienced experts is the simplest method to quantify the CNV lesion. However, this method is subjective, operator intensive, and time-consuming. Therefore, it is valuable to develop a reliable and robust automated detection algorithm for quantifying the CNV lesion.

Due to certain technological limitations and the biologic nature of CNV, there are many issues which need to be addressed regarding automated CNV quantification. Firstly, OCT angiography is susceptible to shadowgraphic flow projection artifacts. Blood vessels cast shadows on deeper structures. Moving blood cells in the blood vessel cast dynamic shadows due to variation in scattering and absorption. This dynamic shadowing causes fluctuation in the intensity of OCT signal from structures under the blood vessels that is detect as decorrelation by the SSADA algorithm. The end result is that the vascular pattern from the superficial inner retina is replicated on the deeper outer retina. Secondly, while the effect of eye motion during the scan can be minimized by subtracting bulk motion noise [13, 20] and using orthogonal registration [21], motion artifacts in the form of horizontal or vertical lines may remain. Finally, the intrinsic complexity of CNV also makes automated detection difficult. The shape, size, location, and velocity of flow of the CNV can vary between participants, and the boundary between CNV and what is not CNV, the background, can be hard to distinguish. Thus, how to deal with artifacts and account for the complexity of the CNV lesion are key problems which need to be solved.

Methods to segment and analyze vascular structures from fundus or FA images have been based on structure enhancement filters [22, 23] and/or geodesic methods [24]. Few works have been published about segmentation of CNV from OCT angiography images [15]. Because the CNV lesion is dissimilar from projection and motion artifacts, we sought to explore saliency based detection methods [25]. Briefly, saliency describes an abstraction of how the human visual system characterizes regions or objects which stand out from their surrounding parts. Saliency based methods attempt to replicate this process for the detection of dominant objects in a scene based on various image features. In this article, we propose an automated algorithm, termed "saliency algorithm," dedicated to CNV recognition in outer retina *en face* angiograms from OCT angiography. The algorithm was tested on scans from 7 participants with neovascular AMD, and the results were compared to output from the algorithm we used previously, termed the "previous algorithm" [15], and results from manual delineation of the CNV.

## 2. Materials and methods

### 2.1 Patient selection and data collection

Participants were recruited from those diagnosed with neovascular AMD at the Casey Eye Institute Retina Service based on clinical presentation, examination, and fluorescein angiography. They were enrolled after informed consent in accordance with an Institutional Review Board/Ethics Committee approved protocol at Oregon Health & Science University and in compliance with the Declaration of Helsinki.

Two volumetric data sets were collected from single eyes of participants with neovascular AMD. All of the data was collected using a commercial 70 kHz spectral domain OCT system with a center wavelength of 840 nm (RTVue-XR, Optovue, CA). The macular angiography scan protocol for a single volumetric data set contained 2 scans covering a $3 \times 3$ mm area. Each scan comprised of $304 \times 304 \times 2$ A-scans acquired in less than 3 seconds. The fast scanning direction was in the horizontal direction for the first scan and in the vertical direction for the second. The SSADA algorithm was applied to detect flow between the 2 consecutive B-scans at the same location [13, 14]. The two scans were then registered and merged through an orthogonal registration algorithm [21].

Sixteen participants were recruited. Data from 6 participants were excluded due to low image quality (structural OCT signal strength index <50), severe motion artifacts, and/or shadowing due to pigment epithelial detachment. Data from 3 other participants were excluded because an experienced grader could not identify the presence of CNV on OCT angiography. Data from the remaining 7 participants were used in this study.

*2.2 Algorithm overview*

An overview of the developed algorithm is shown in Fig. 1. A pre-processing step was first performed to reduce projection artifacts from the outer retina. After denoising, the CNV region was more distinctive. Vascular pattern recognition through a saliency model followed. Finally, post-processing steps based on nonlinear filtering, thresholding, and morphological operations were applied to generate the CNV membrane mask. The following three sections will describe the process in detail. The algorithm was implemented with custom software written in Matlab 2011a (Mathworks, Natick, MA).
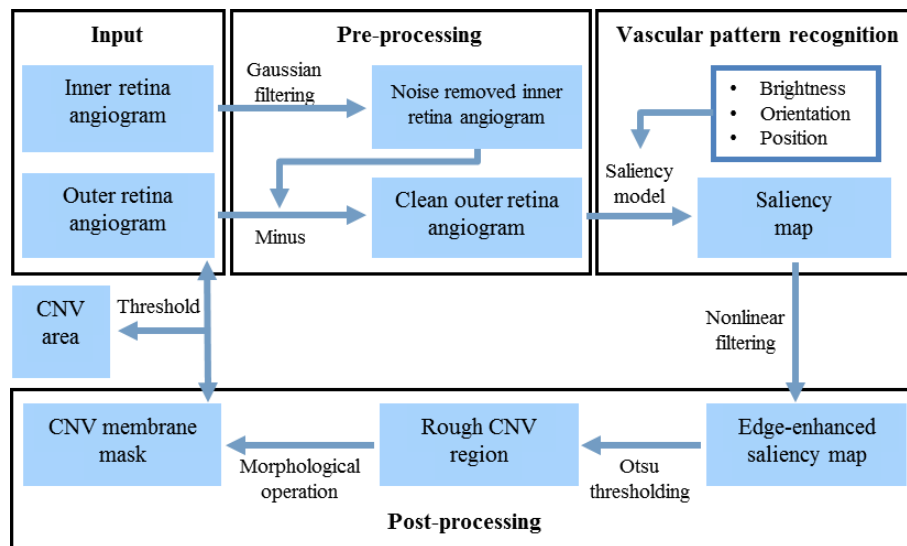


Fig. 1. Overview of the developed choroidal neovascularization (CNV) detection algorithm.

*2.3 Pre-processing*

Retinal circulations are primarily transverse to the OCT light beam and are best visualized by projecting the volumetric data set as 2D *en face* images. Anatomical landmarks from structural OCT images were used to guide semi-automated segmentation to separate circulations based on depth [26]. Maximum flow projection between the internal limiting membrane (ILM) and outer plexiform layer (OPL) generated the *en face* inner retinal angiogram. Maximum flow projection between the outer boundary of OPL to BM generated the *en face* outer retinal angiogram, normally an avascular region. CNV grows from the

choroid through BM and often is directly adjacent to the retinal pigment epithelium (RPE). Inner retinal vessels project artifact onto the RPE, due to its high reflectance on structural OCT. Projection artifacts in the outer retinal angiogram interfere with CNV detection.

Angiographic projection and motion artifacts ideally need to be minimized prior to application of the saliency method. In previous work [15], we used a binary large inner retinal vessel map to mask vessel projections on the outer retinal angiogram. However, it can be hard to determine the threshold for obtaining such a vessel mask. If the threshold value is low, the mask would contain smaller inner retinal vessels which could remove some useful information in the CNV region. Alternatively, masking just large vessels may leave small inner retinal vessel projections that are hard to differentiate as projection artifact or CNV. In this algorithm, the inner retinal angiogram was filtered by a $20 \times 20$ pixel Gaussian filter with a sigma of 0.1. The filtered inner retinal angiogram was then subtracted from the outer retinal angiogram. The resulting image better highlighted the CNV region, but still contained small, bright discrete noise areas.

## 2.4 Vascular pattern recognition

Because the CNV becomes more distinct in the outer retinal angiogram after artifact removal, saliency based detection could be an effective and robust method. Detection accuracy depends on both the distinctiveness of the target object and the homogeneity and/or blurred degree of the background. As a result of projection removal, some parts of the CNV region became discontinuous and fuzzy. Therefore, the saliency model should detect not only the salient region and but also neighboring regions. Context-aware saliency detection described by Goferman, et al. may be able to account for the above issues. This method combines context-awareness and saliency detection with the aim of identifying prominent objects and parts of the background that contain similar contextual information [27].

Context-aware saliency detection borrows from some basic principles associated with human visual attention: local low-level considerations such as brightness and contrast, global considerations to ignore reoccurring features, and visual organization rules regarding object center(s) of gravity. For many image processing applications, local and global considerations incorporate color information, but OCT angiography is simplified in a way as it produces what can be considered grayscale *en face* images. Here, brightness, orientation contrast, and positional distance were used together to define distinctiveness. In the *en face* outer retinal angiogram, each pixel $i$ was assessed. The local context of pixel $i$ was given by considering its surrounding pixels in a $7 \times 7$ pixel patch centered on the pixel. The saliency of each pixel $i$ depends on the distinctiveness of its patch. We defined $d_{bright}(p_i, p_j)$ as the Euclidean distance between the summed intensities of patches $p_i$ and $p_j$ in the grayscale image, normalized to the range [0,1].

However, because there were still some small, bright non-CNV areas in the projection removed angiogram, brightness information alone was not enough. Therefore, the local orientation information [28] was incorporated to aid in the determination of what is of interest. The local orientation information was obtained utilizing Gabor filters, which are a product of a cosine grating and 2D Gaussian envelope, at four preferred orientations $\theta \in \{0°, 45°, 90°, 135°\}$. The size of the Gabor kernel was $31 \times 31$ pixels. The Euclidean distance $d_{orientation}(p_i, p_j)|_\theta$ between patches $p_i$ and $p_j$ was calculated as the orientation contrast at the corresponding orientation $\theta$:

$$d_{orientation}\left(p_i, p_j\right) = \frac{1}{N}\sum d_{orientation}\left(p_i, p_j\right)\big|_\theta \qquad (1)$$

where $\theta = 0°, 45°, 90°, 135°$ and N = 4. This was also normalized to the range [0,1]. In the projection removed outer retinal angiogram, CNV regions were grouped together. Thus, let $d_{position}(p_i, p_j)$ be the positional distance between patches $p_i$ and $p_j$. The distinctiveness between two patches is then defined as

$$d(p_i, p_j) = \frac{d_{bright}(p_i, p_j) + d_{orientation}(p_i, p_j)}{2(1 + c \cdot d_{position}(p_i, p_j))} \tag{2}$$

where $c = 3$. The distinctiveness measure considers the local and global information simultaneously. It is proportional to the difference in appearance represented by brightness and orientation contrast and inversely proportional to positional distance. Pixel $i$ is considered salient when $d(p_i, p_j)$ is high for all $j$.

Multi-scale saliency detection was further incorporated to decrease the saliency of background and enhance the contrast between salient and non-salient areas. Typically, background patches are more likely to be similar at multiple scales, while the dominant object is salient and could have similar patches at a few scales but not at all of them. Because using multiple scales increases computation time, we simplified the comparisons to only the $K$ most similar patches. The saliency value of pixel $i$ at a single-scale $r$ was then defined as

$$S_i^r = 1 - \exp\{-\frac{1}{K}\sum_{k=1}^{K} d(p_i^r, q_k^r)\} \tag{3}$$

where $q_K$ belongs to the identified $K$ most similar patches and $K = 65$. When searching for the $K$ most similar patches, patches of $7 \times 7$ with 50 percent overlap were considered.

The saliency of pixel $i$ at scale $r$ was determined from the $K$ most similar patches at multiple scales $R_q = \{r, (1/2)r, (1/4)r\}$. At each scale $r$, the saliency map was normalized to the range [0,1] and interpolated back to original image size of $304 \times 304$ pixels. Equation (3) was refined as

$$S_i^r = 1 - \exp\{-\frac{1}{K}\sum_{k=1}^{K} d(p_i^r, q_k^{r_k})\} \tag{4}$$

where $r_k \in R_q$. The final saliency value for pixel $i$ was the mean of all patches $p_i$ at different scale $r$.

$$\bar{S}_i = \frac{1}{M}\sum_{r \in R} S_i^r \tag{5}$$

Four scales were used, $R = \{100\%, 80\%, 50\%, 30\%\}$.

One final consideration was that areas close to the attention foci are supposed to be more distinctive than those regions far away. The visual contextual effect was simulated. A threshold operation was applied to extract the most attended localized areas from the saliency map, which contained all the pixels with their saliency value greater than a threshold of 0.8. The saliency value of pixels outside the most attended localized areas was redefined according to its Euclidean distance $d_{foci}^r(i)$ of position to the closest attended pixel at scale $r$, normalized to range [0,1]. The saliency of each pixel was modified as

$$\hat{S}_i = \frac{1}{M}\sum_{r \in R} S_i^r (1 - d_{foci}^r(i)) \tag{6}$$

After this step, the saliency value of the interesting background in the neighborhood of salient objects will be increased. This allowed for the inclusion of neighboring regions to ensure all of the CNV was detected.

*2.5 Post-processing*

The integration of multi-scale enhancement and context-awareness led to a saliency map that approximated the CNV region. However, it was hard to determine the threshold to extract the CNV region from the saliency map as the map was usually blurred at its boundaries. To do so,

we first used a Laplacian edge detection filter on the saliency map. In parallel, the bilateral filter proposed by Tomasi, et al. [29] was used to smooth within the target region and preserve the boundary. This bilateral filter was a weighted average operation process. Unlike the traditional Gaussian filter which utilizes just positional information as the weight, the weight of the shift-invariant Gaussian filter belonging to the bilateral filter contains both positional distance and intensity information. After bilateral filtering, the boundary information detected by the Laplacian edge detection operator was used to enhance the boundaries. Otsu's threshold method was used to extract the rough CNV region. Some small discrete regions still remained. Morphological operations were then used to remove small areas (<80 pixels) and fill holes. Finally, the CNV membrane mask was obtained. It was a binary image by which the original *en face* outer retinal angiogram was multiplied to extract the CNV. A threshold operator was used to calculate the CNV area.

*2.6 Verification of results*

We assessed within-visit repeatability of the previous automated algorithm, saliency algorithm, and manual delineation using coefficient of variation (CV) and intraclass correlation (ICC). For manual delineation, the CNV boundary was contoured by an experienced grader, and a threshold operator was used to calculate the CNV area.

To compare the results from the two automated algorithms to results from manual delineation, we used the Jaccard similarity metric, which is defined as

$$J(I_s, I_m) = \frac{|I_s \cap I_m|}{|I_s \cup I_m|} \tag{7}$$

where $I_s$ is the segmentation result from one of the automated pipelines and $I_m$ is the result from manual delineation. The Jaccard coefficient ranges from 0 to 1, where 1 denotes the two were identical and 0 if they were completely dissimilar. Using the manual delineation results as the standard, errors rates were also computed. False positive error was the ratio of the total number of automatically segmented pixels that were not included in the manual segmentation result to the total number of manually segmented pixels. False negative error was the ratio of the total number of manually segmented pixels that were not included in the automated segmentation result to the total number of manually segmented pixels [30].

## 3. Results

The *en face* outer retinal angiogram from a participant with neovascular AMD was used as an example to show the workflow of the previous algorithm and saliency algorithm. Figure 2(A) shows the original outer retinal angiogram with CNV and artifacts. The left column illustrates the steps of the previous algorithm. The mask of inner retinal vessels shown in Fig. 2(B1) was used to remove the large vessels projections from the outer retina. The result shown in Fig. 2(C1) still has some small vessel projections and motion artifacts. The previous algorithm then applied a Gaussian filter to reduce the remaining artifacts (Fig. 2(D1)). For the final step, a threshold operator was used to extract the CNV area (Fig. 2(E1)). However, artifacts remained after the mask subtraction and thresholding, leading some to be misclassified as CNV. In the saliency algorithm, the inner retinal angiogram was first smoothed by a $20 \times 20$ pixel Gaussian filter to produce the filtered inner retina shown in Fig. 2(B2). By subtracting the filtered inner retina from the outer retina, most of the projection artifacts were removed (Fig. 2(C2)) and some CNV signal was also reduced. However, the CNV area became more distinctive in the outer retina. Then, a context-aware saliency model based on brightness, orientation, and position information was used to detect the CNV region (Fig. 2(C2)). The saliency calculation was done at multiple scales (Fig. 2(F1)) and combined into a single saliency map (Fig. 2(D2)). To aid in the segmentation of the CNV, an edge-enhanced nonlinear filter was used to smooth the CNV region and enhance the boundary. Next, Otsu's

method was used to determine the threshold. Finally, morphological operations were used to remove small isolated regions and fill holes to obtain the CNV membrane mask. These post-processing steps are shown in Fig. 2(F2). The *en face* outer retinal angiogram was multiplied by the CNV membrane mask, and a threshold operator was used to determine the CNV area (Fig. 2(E2)).
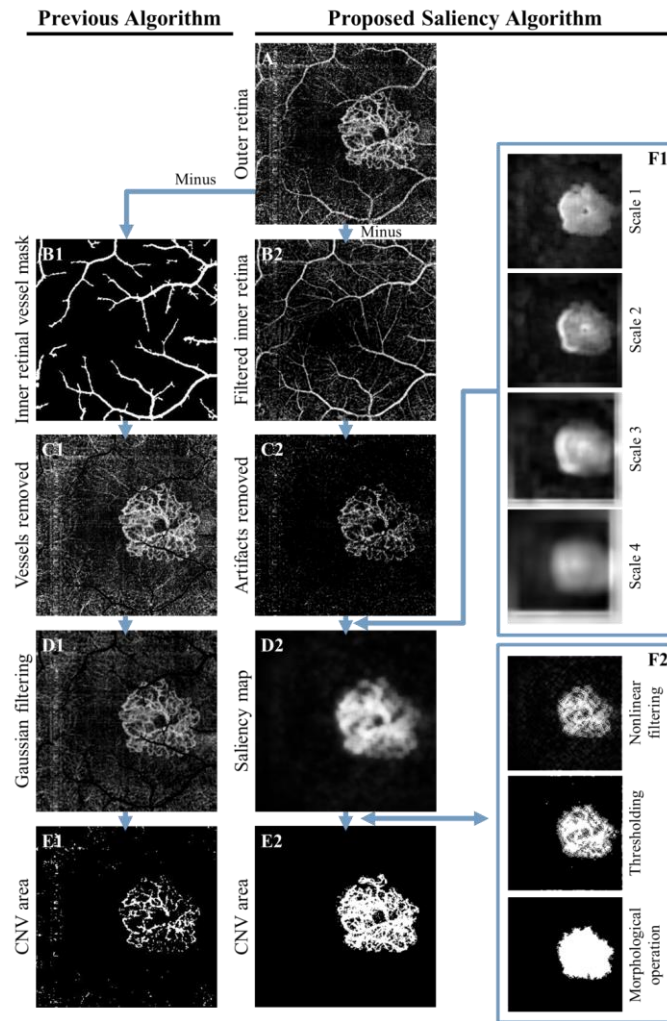


Fig. 2. The previous automated choroidal neovascularization (CNV) segmentation algorithm and proposed saliency algorithm. (A) Original outer retinal angiogram from a participant with neovascular age-related macular degeneration (AMD) showing artifacts and CNV. (B1) Inner retinal large vessel mask used to subtract large vessel projections from the outer retina. (B2) Filtered inner retina used to subtract artifacts from the outer retina. (C1) Outer retina with large vessel projections removed. (C2) Outer retina with artifacts removed. (D1) Gaussian filtering with the aim to reduce the remaining artifacts. (D2) Saliency map showing the CNV region. (E1) CNV area obtained by a threshold operator. (E2) CNV area obtained by multiplying the CNV membrane mask and original *en face* outer retinal angiogram and using a threshold operator. (F1) Multi-scale saliency results showing intermediate results of calculating the saliency map. (F2) Post-processing procedure including nonlinear filtering to enhance the boundaries and smooth the saliency map, Otsu's method for determining the threshold, and morphological operations for obtaining the CNV membrane mask. (A, B2, C1, C2, D1) The display scale of decorrelation values ranges from 0.025 to 0.25.

The results from the saliency algorithm were compared with results from the previous automated algorithm and manual delineation of the CNV. Data from a single eye of 7 participants with neovascular AMD were analyzed. Two volumetric data sets from each eye were evaluated to assess within-visit repeatability. The results from one volumetric data set are shown in Figs. 3 and 4. The cases included both type I and type II (participants #1, 5) CNV membranes with a wide range of sizes. An expert human grader delineated the boundary of the CNV membrane on the *en face* maximum flow projection angiogram of the outer retinal slab, while also viewing the inner retinal angiogram. The saliency algorithm automatically outlined the CNV boundary and calculated CNV area. The algorithm required 17.5 seconds to execute on an Intel Xeon CPU (E3-1226, 3.3 Ghz), of which 94% of the time was spent on generating the saliency map.
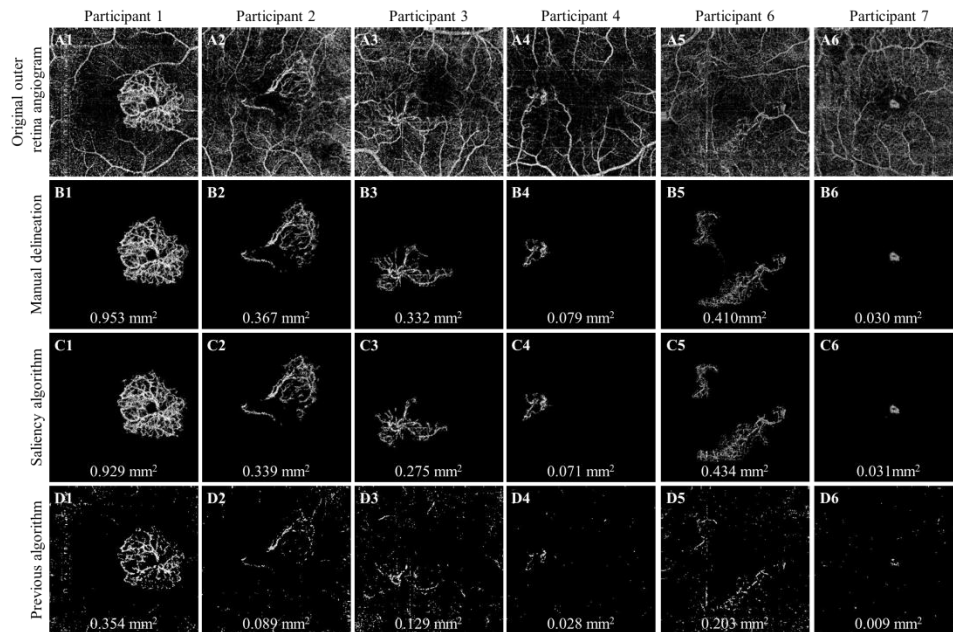


Fig. 3. *En face* OCT angiograms from all participants except for #5 which is shown in Fig. 4. The top row (A1-7) shows the *en face* maximum flow projection angiogram from the outer retinal slab without any additional processing. The second row (B1-5) shows the results of manual delineation of CNV by an expert human. The third row (C1-5) shows the results from the automated saliency algorithm. The bottom row (D1-5) shows the results from the previous automated algorithm. CNV areas, as delineated by a grader or algorithm, are shown below each processed image. The display scale of decorrelation values ranges from 0.025 to 0.25 for all images.
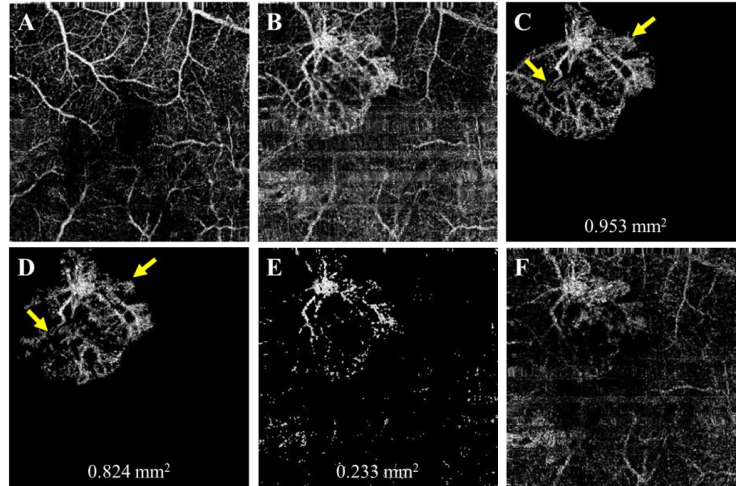
Fig. 4. *En face* OCT angiograms from the case (participant #5) where there was the greatest difference in CNV area between the saliency algorithm and expert manual grading. (A) Inner retinal angiogram. (B) Outer retinal angiogram without any additional processing. (C) Manual delineation of CNV by an expert human. (D) Automated saliency algorithm. Yellow arrows highlight points of interest for comparison between C and D. (E) Previous automated algorithm. CNV areas, as delineated by a grader or algorithms, are shown below each processed image. (F) Choriocapillaris angiogram without any additional processing. The display scale of decorrelation values ranges from 0.025 to 0.25 for all images.

Qualitatively, the results from the saliency algorithm were closely matched to that from manual delineation. However, the saliency algorithm tended to include less area from the CNV due to the projection artifact removal step. This is highlighted in the results from participant #5 in Fig. 4 (compare the respective regions as indicated by yellow arrows in Figs. 4(C) and 4(D)). The previous algorithm also identified similar shapes for the CNV membranes, but did not cleanly remove scattered background noise due to projection and motion artifacts. The continuity of the CNV network was also often broken up by the higher decorrelation threshold used. It was clear that the previous algorithm differed more from manual CNV grading, and this poor agreement was reflected in the Jaccard similarity metric, false negative, and false positive CNV pixel identification rates (Table 1). In contrast, the saliency algorithm agreed well with manual grading. The saliency algorithm was significantly better than the previous algorithm in all measures of agreement with manual grading (Table 1).

**Table 1. Agreement Between Automated Algorithms and Manual Grading of Choroidal Neovascularization**

|  | Proposed saliency algorithm | Previous algorithm | P-value |
|---|---|---|---|
| **Jaccard similarity metric** | $0.834 \pm 0.125$ | $0.157 \pm 0.059$ | <0.001 |
| **False positive error** | $0.043 \pm 0.046$ | $0.120 \pm 0.066$ | 0.001 |
| **False negative error** | $0.134 \pm 0.109$ | $0.826 \pm 0.059$ | <0.001 |

Measures of agreement were computed on a pixel-by-pixel basis from graded *en face* angiograms of choroidal neovascularization. Mean ± standard deviation of the Jaccard similarity metric and error rates were computed from 7 participants. P-values were based on the paired Wilcoxon rank-sum test.

Repeatability of CNV area measurement was calculated from the 2 sets of OCT angiography scans obtained from each participant. All methods had relatively good repeatability as measured by CV and ICC (Table 2).

**Table 2. Repeatability of Choroidal Neovascularization Quantification**

|  | Manual | Proposed saliency algorithm | Previous algorithm |
|---|---|---|---|
| **CV** | 3.90% | 6.70% | 7.15% |
| **ICC** | 0.998 | 0.992 | 0.993 |

Abbreviations: coefficient of variation (CV); intraclass correlation (ICC). Data was from 7 participants.

## 4. Discussion

OCT angiography is a new imaging approach to visualizing CNV. Herein, we proposed an algorithm for CNV area quantification which involves 4 main steps: (1) minimize projection artifacts in the outer retinal angiogram by subtracting the inner retinal vessel pattern; (2) identify the CNV area by a context-aware saliency model based on brightness, orientation, and position information; (3) enhance the saliency map by nonlinear filtering; and (4) calculate CNV area from flow pixels within the CNV boundary. We showed that the proposed algorithm could detect and quantify the CNV in neovascular AMD cases with a variety of CNV patterns. The saliency algorithm agreed with expert human grading much better than the previous automated algorithm. The previous algorithm had a notably high false negative rate of 0.826 (Table 1) because the steps of subtracting large inner retinal vessel projection and thresholding also removed flow signal in the CNV. Identification of the CNV through the saliency map helped to restore the outline of the CNV after removal of projection artifact.

The previous algorithm had worked well using OCT angiography obtained using a 1050 nm swept-source OCT system. The projection artifact from the inner retinal vessel onto the outer retina was much sparser at the longer wavelength [15], and consisted of mainly a large vessel pattern, therefore the CNV pattern was not as severely disrupted by the projection artifact. In the 840 nm spectral domain OCT system employed in the current study, the shadow cast by the inner retinal vessels was much stronger due to the shorter wavelength. Therefore the projection artifact included not only larger retinal vessels but also fine capillary patterns. The removal of this much denser projection artifact disrupted the CNV pattern much more severely. Therefore the saliency map was needed to restore the CNV outline. The Gaussian filter and thresholding employed by the previous algorithm were not adequate to the task. Figure 5 illustrates the problem with dense inner retinal projection. Both the subtraction of all projection artifacts and the saliency map steps were necessary to obtain a clean outline of the CNV.
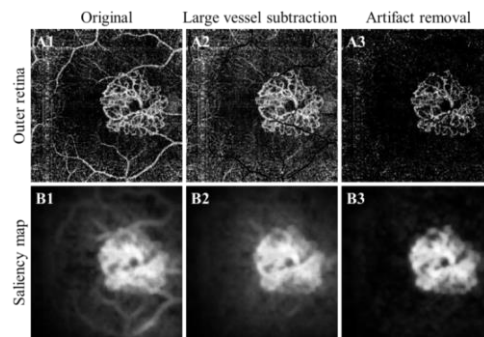


Fig. 5. (A1) Original outer retinal angiogram. (A2) Outer retinal angiogram with inner retinal large vessel subtracted leaving motion artifacts and small vessel projections. (A3) Outer retinal angiogram with both large and small retinal vessels subtracted. (B1) Saliency map computed from A1 shows the CNV outline but is contaminated with large retinal vessel pattern. (B2) Saliency map computed from A2 shows CNV outline but is cluttered with a background haze. (B3) Saliency map computed from A3 shows a clean CNV pattern. (A1 to A3) The display scale of decorrelation values ranges from 0.025 to 0.25.

Due to the vessel pattern of CNV also projecting onto deeper structures, we and others have noted that CNV could also be identified from the choriocapillaris or inner choroidal angiograms [17, 31]. In a healthy eye, the choriocapillaris typically shows nearly confluent flow. In cases of neovascular AMD, the CNV pattern in choriocapillaris angiogram (Fig. 4(F)) can be quite similar to what is observed in the outer retinal angiogram. In addition, it is often surrounded by a negative halo of reduced flow, which may be useful in highlighting the CNV pattern in relief. Automated CNV quantification in the choriocapillaris angiogram is likely possible using the saliency algorithm, but alternative strategies that make use of the negative halo may be worth exploring.

While the saliency algorithm was effective at quantifying CNV in this small group of participants, additional studies with a larger number of participants with CNV are needed. The algorithm needs to be tested in participants with highly reflective pathologies such as drusens or exudate, which could potentially accentuate projection artifacts and fool the algorithm into false positive identification of CNV [32]. Beyond computing CNV area in eyes known to have CNV, the algorithm could also be used to distinguish eyes with CNV from both healthy eyes and eyes with non-neovascular AMD. Longitudinal studies to monitor the CNV or track its change in response to treatment would also be valuable.

## 5. Conclusion

We developed a saliency-based automated algorithm to identify CNV on outer retinal angiograms. The algorithm removed inner retinal vessel projection artifacts, and identified a clean outline of CNV using a saliency model based on intensity, orientation, and position information. Results from the algorithm agreed well with results from manual delineation of CNV by both visual inspection and quantitative metrics.

## Acknowledgments